

AD-A158 684

Precision Interferometric Dilatometer

E. G. WOLFF and R. C. SAVEDRA
Materials Sciences Laboratory
Laboratory Operations
The Aerospace Corporation
El Segundo, CA 90245

12 August 1985

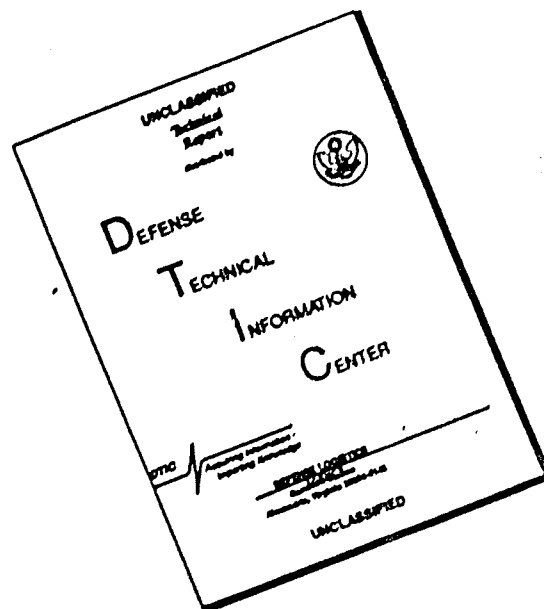
APPROVED FOR PUBLIC RELEASE;
DISTRIBUTION UNLIMITED

DTIC
SELECTED
AUG 29 1985
S D G

DTIC FILE COPY

Prepared for
SPACE DIVISION
AIR FORCE SYSTEMS COMMAND
Los Angeles Air Force Station
P.O. Box 92960, Worldway Postal Center
Los Angeles, CA 90009-2960

DISCLAIMER NOTICE



THIS DOCUMENT IS BEST QUALITY AVAILABLE. THE COPY FURNISHED TO DTIC CONTAINED A SIGNIFICANT NUMBER OF PAGES WHICH DO NOT REPRODUCE LEGIBLY.

This report was submitted by The Aerospace Corporation, El Segundo, CA 90245, under Contract No. F04701-83-C-0084 with the Space Division, P.O. Box 92960, Worldway Postal Center, Los Angeles, CA 90009-2960. It was reviewed and approved for The Aerospace Corporation by R. W. Fillers, Director, Materials Sciences Laboratory.

Capt Stephen H. Doerr/YV was the project officer for the Mission-Oriented Investigation and Experimentation (MOIE) Program.

This report has been reviewed by the Public Affairs Office (PAO) and is releasable to the National Technical Information Service (NTIS). At NTIS, it will be available to the general public, including foreign nationals.

This technical report has been reviewed and is approved for publication. Publication of this report does not constitute Air Force approval of the report's findings or conclusions. It is published only for the exchange and stimulation of ideas.

Stephen H. Doerr

STEPHEN H. DOERR, Capt, USAF
MOIE Project Officer
SD/YVE

Joseph Hess

JOSEPH HESS, GM-15
Director, AFSTC West Coast Office
AFSTC/WCO OL-AB

Accession For	
NTIS GRA&I	<input checked="checked" type="checkbox"/>
DTIC TAB	<input type="checkbox"/>
Unannounced	<input type="checkbox"/>
Justification	
By	
Distribution/	
Availability Codes	
Dist	Avail and/or Special
A/1	



UNCLASSIFIED

SECURITY CLASSIFICATION OF THIS PAGE (When Data Entered)

REPORT DOCUMENTATION PAGE		READ INSTRUCTIONS BEFORE COMPLETING FORM
1. REPORT NUMBER SD-TR-85-47	2. GOVT ACCESSION NO. A158684	3. RECIPIENT'S CATALOG NUMBER
4. TITLE (and Subtitle) PRECISION INTERFEROMETRIC DILATOMETER		5. TYPE OF REPORT & PERIOD COVERED
7. AUTHOR(s) Ernest G. Wolff and Raymond C. Savedra		6. PERFORMING ORG. REPORT NUMBER TR-0084A(5935-12)-1
9. PERFORMING ORGANIZATION NAME AND ADDRESS The Aerospace Corporation El Segundo, Calif. 90245		8. CONTRACT OR GRANT NUMBER(s) F04701-83-C-0084
11. CONTROLLING OFFICE NAME AND ADDRESS Space Division Los Angeles Air Force Station Los Angeles, Calif. 90009-2960		10. PROGRAM ELEMENT, PROJECT, TASK AREA & WORK UNIT NUMBERS
14. MONITORING AGENCY NAME & ADDRESS (if different from Controlling Office)		12. REPORT DATE 12 August 1985
		13. NUMBER OF PAGES 31
		15. SECURITY CLASS. (of this report) Unclassified
		15a. DECLASSIFICATION/DOWNGRADING SCHEDULE
16. DISTRIBUTION STATEMENT (of this Report) Approved for public release; distribution unlimited.		
17. DISTRIBUTION STATEMENT (of the abstract entered in Block 20, if different from Report)		
18. SUPPLEMENTARY NOTES		
19. KEY WORDS (Continue on reverse side if necessary and identify by block number) Dilatometry; Michelson interferometry; Signal processing; Thermal expansion.		
20. ABSTRACT (Continue on reverse side if necessary and identify by block number) An improved double Michelson laser interferometric dilatometer with an inexpensive automatic signal processor is described. The unit is suitable for studying materials having near-zero coefficients of thermal expansion (CTE) ranging from 100 to >450 K. $\Delta L/L$ values to a resolution of 10^{-8} and instantaneous CTE values (to $<10^{-8}$ K ⁻¹) can be plotted in real time at regular intervals (>30 s) to give time-related absolute expansion data of noncontacted samples of arbitrary shape or size. <i>keep in file</i>		

DD FORM 1473
(FACSIMILE)

UNCLASSIFIED

SECURITY CLASSIFICATION OF THIS PAGE (When Data Entered)

PREFACE

The authors wish to acknowledge the help of W. H. Dittrich in the operation and testing of the interferometer.

CONTENTS

PREFACE.....	1
I. INTRODUCTION.....	5
II. DILATOMETER DESCRIPTION.....	7
A. Optics.....	7
B. Sample Support.....	9
C. Error Analysis.....	9
D. Operational Procedure.....	12
III. SIGNAL PROCESSING.....	13
IV. AC COUNTER ELECTRONICS.....	17
V. DATA PROCESSING.....	27
VI. CONCLUSIONS.....	29
REFERENCES.....	31

FIGURES

1.	Diagram of the Double Michelson Interferometer Optics.....	8
2.	Variation of Radial ΔT with Heating and Cooling Rate.....	11
3.	Block Diagram of the Test Setup for the Interferometric Dilatometer.....	14
4.	Schematic of the Interferometer Signal Conditioner ($\times 4$ for Double Michelson).....	16
5.	Schematic of the Clipper Circuit.....	18
6.	Schematic of the A Quad B Counter and the D/A Converter.....	19
7.	Schematic of the Steering Logic Circuit.....	20
8.	Diagram of the Directional Counting Sequence.....	22
9.	Interferometric Counter Output as Voltage Applied to PZT-Driven Mirror ($1000 \text{ V} \equiv 15 \text{ } \mu\text{m}$ motion).....	24
10.	Interferometric Counter Output vs. Voltage Applied to PZT-Driven Mirror (fine scale).....	25
11.	Counter Output vs. Micrometer Displacement.....	26
12.	Thermal Strain and Instantaneous CTE vs. Temperature for a Fused-Silica Rod.....	28

TABLE

1.	Logic Circuit Evaluation.....	21
----	-------------------------------	----

I. INTRODUCTION

Michelson interferometry is widely used to detect small, even sub-angstrom, displacements¹⁻³ (e.g., in piezoelectric transducer calibration⁴), but has seen limited application in the measurement of thermally induced expansions. Earlier methods were subject to complexity, differential techniques, nonuniform temperature gradients, and/or expense.⁵⁻⁷ A double Michelson interferometer was developed³ that is capable of measuring coefficients of thermal expansion (CTEs) of arbitrarily shaped samples, ranging in temperature from 100 to 450 K to a resolution of $<10^{-8} \text{ K}^{-1}$.

The large number of optics components (over 30) required lengthy alignment procedures, and special features were needed to accommodate temperature effects on the optics. Since both interferometers were actually in vacuo, a complex remote beam-steering device would be needed to account for sample movements during an experiment. (Problems with this approach are outlined by Drotning.⁷) In subsequent work some advantages of phase modulation over polarization effects for automated signal processing were explored.^{8,9} In the latter system, the harmonics of the modulated fringe pattern, detected by a single photodetector, are compared to generate the required phase information. Drawbacks included a requirement of $>1 \text{ kHz}$ modulation frequency to achieve adequate immunity from sample vibration-induced noise. This in turn required piezoelectric transducers (PZTs) to operate at their resonant frequencies for adequate depth of modulation.

This report describes improvements in both the optics and signal processing of such an interferometer, with major objectives being reductions in cost and set-up time, and an increase in ease of operation. A new data-reduction feature is time information, in recognition of the fact that low thermal expansion values are significantly modified by the samples' finite thermal diffusivity and internal stress-relaxation mechanisms (such as micro-cracking or plastic flow in composite materials).

II. DILATOMETER DESCRIPTION

A. OPTICS

Figure 1 illustrates the basic features of a double Michelson interferometer. The optics were simplified from those described in Ref. 3 by bringing the beamsplitters (B_1 and B_2) and sample-beam steering mirrors (P_1 and P_2) outside the vacuum system to allow rapid signal adjustments should the sample move. The optics components inside the vacuum chamber are limited to the reference mirrors (M_1 and M_2) and the sample reflections (S_1 and S_2). If we denote the left-hand interferometer as 1 in Fig. 1, and the other as 2, it is seen that the optical path-length differences (OPLD) are given by

$$\text{OPLD}_1 = 2(\overrightarrow{B_1 M_1} - \overrightarrow{B_1 P_1 S_1}) \quad (1)$$

$$\text{OPLD}_2 = 2(\overrightarrow{B_2 M_2} - \overrightarrow{B_2 P_2 S_2}) \quad (2)$$

The factor of 2 comes from the fact that the optical path is twice the geometrical path. By symmetry,

$$\overrightarrow{B_1 M_1} + L_u + \overrightarrow{M_2 B_2} = \overrightarrow{P_1 S_1} + L_s + \overrightarrow{S_2 P_2} \quad (3)$$

and

$$\overrightarrow{B_1 P_1} = \overrightarrow{B_2 P_2} \quad (4)$$

Adding the two OPLDs, substituting $B_1 M_1$ from Eq. (3), and using Eq. (4) gives

$$L_s = \frac{\text{OPLD}_1 + \text{OPLD}_2}{2} + L_u + 2(\overrightarrow{P_1 B_1}) \quad (5)$$

L_s and L_u are the sample length and width of the reference mirrors ($M_1 - M_2$), respectively. The use of reflective mirrors, such as ULE (Corning Code 7971 ultra-low-expansion glass), on the ends of the sample increases L_s to $(L_s + L_1 + L_2)$.

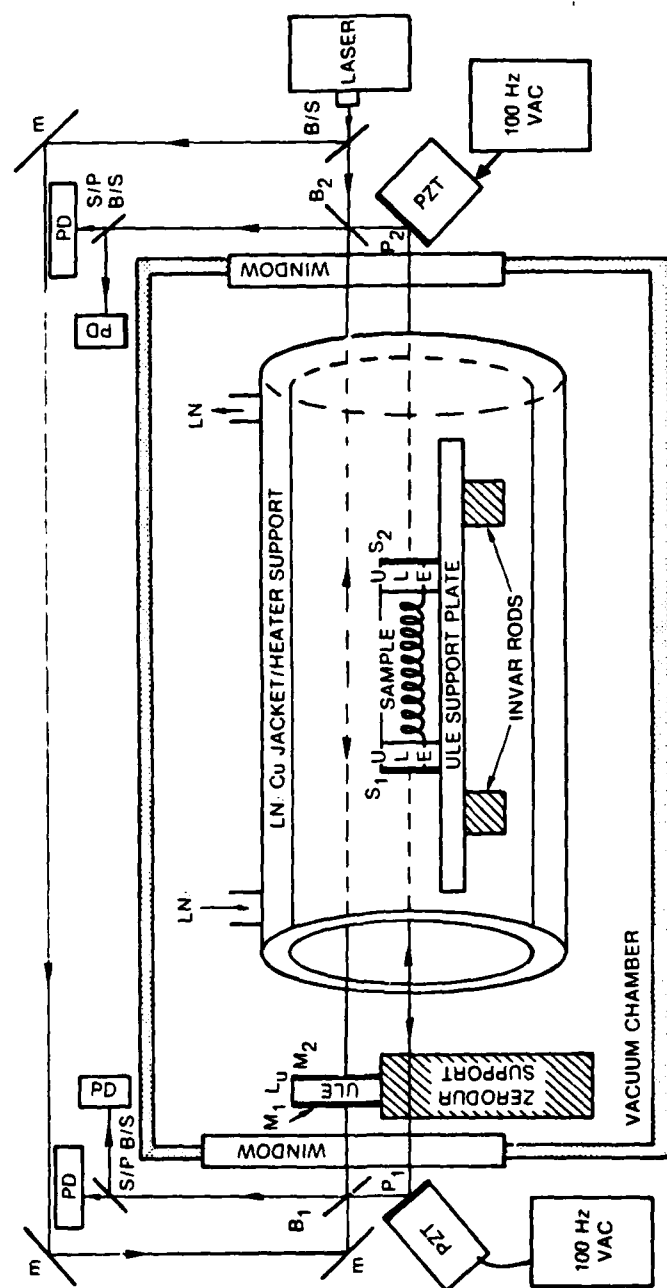


Figure 1. Diagram of the Double Michelson Interferometer Optics

Accurate measurement of a change in sample length requires a zero or known length change in L_u and $\overrightarrow{B_1P_1}$. The first is accomplished by mounting the reference mirrors on a ULE glass or Zerodur block in a thermally insulated part of the system. Since the B_1P_1 (or B_2P_2) paths are in air, mounting must compensate for index-of-refraction changes (see Section II.C). Sample end movement may be caused by the bowing of an unsymmetrical laminate. In this case, short-focal-length lenses³ are symmetrically positioned (for equal heat effects) to focus the beams on both sample and reference-mirror surfaces. Preferably, the normal dispersion of a single-frequency He-Ne laser beam can be modified with lenses or collimators to achieve focus on the sample ends without the need for lenses in the vacuum chamber.

B. SAMPLE SUPPORT

The sample-support system required to maintain the axis of the sample parallel to the laser beams between the PZT mirrors (Fig. 1) has been described.^{3,10} The end faces of the sample must be flat and perpendicular to this axis to within a few tenths of a degree. They are polished and coated with a thin layer of Al, Au, or Cr. ULE glass end mirrors for porous samples are spring loaded, as cements tend to shift the mirrors. The apparatus of Fig. 1 handles samples of any size, with laser beam spacing, spot size, and uniform temperature being limitations. Modifications for larger samples have been described elsewhere.^{2,11} Temperature measurement is accomplished with two 2-mil Cu-Constantan thermocouples. They must be loosely positioned to prevent them from moving small samples during heating and cooling.

C. ERROR ANALYSIS

The rectangular beam arrangement in Fig. 1 provides immunity from errors resulting from uniform support-table contraction and expansion. If the beams $\overrightarrow{S_1P_1}$ and $\overrightarrow{M_1B_1}$ are not quite parallel, errors are still small. For example, if the beam strikes one sample end 2.5 mm from the parallel beam point, and the (steel) table heats or cools 5°C during an experiment, the net measurement error is about 5 Å. Index-of-refraction changes in the vacuum chamber are negligible if a diffusion pump is used. Drift is caused by room-temperature

changes in the external optics. The major source of error is the air paths $\overline{B_1P_1}$ and $\overline{B_2P_2}$. The temperature-induced change in optical path length (OPL) is

$$\Delta OPL = 2\Delta T (\partial \overline{B_1P_1} / \partial T) = 2\Delta T [\alpha l_a + (\partial n / \partial T) l_b] \quad (6)$$

where l_a and l_b represent the mechanical connections and air distances, respectively, and α the CTE of the total support system. The largest term is $\partial n / \partial T$ of air, about $-9.33 \times 10^{-7} \text{ K}^{-1}$ in the vicinity of 22°C , 50% R.H., and 1000 mb.¹² If $l_b = 12 \text{ mm}$, then αl_a should be $\sim 4.6 \times 10^{-7} \text{ K}^{-1}$ for a zero error. A fused-silica support is suggested. With a Zerodur support (lower α) a typical drift rate of $\lambda/20 \text{ h}^{-1}$ is encountered in a room that fluctuates by 3 to 4°C/day . For more precise work, these components (B and P) can be moved into the vacuum chamber.

The reference mirror support (e.g., Zerodur) is shielded from temperature excursion, and a conservative error is

$$\Delta L_u = \alpha L_u \Delta T = (1 \times 10^{-7}) (3 \times 10^{-3}) (5) = 15 \times 10^{-10} \text{ m (15 \AA)} \quad (7)$$

Temperature gradients in the support table could cause bowing and a change of $\overline{B_1B_2}$ relative to $\overline{P_1P_2}$.^{2,3} This error, equivalent to ΔL_u in Eq. (3), has been transferred from the Zerodur plate in the vacuum chamber³ to the external optical bench. The error is kept negligible by insulating the heater/cooler from this bench and minimizing the beam separation (e.g., 10 mm) in Fig. 1. Lenses introduce errors if they change temperature, typically 100 Å for each degree K change.³ Temperature gradients in the sample cause errors in two ways: (a) by giving a false average temperature reading (with thermocouples) and (b) by distorting the end faces. Figure 2 illustrates the temperature difference between the surface and center of typical test samples as a function of heating/cooling rates. At a typical 2°C/min rate, errors are $\sim 0.1^\circ\text{C}$. The sample end faces will become parabolic, and the position of the beam determines the relative error. It can be shown that this error is a maximum of $\sim \alpha_s \Delta T / 3$, where α_s is the sample CTE and ΔT is found from Fig. 2.

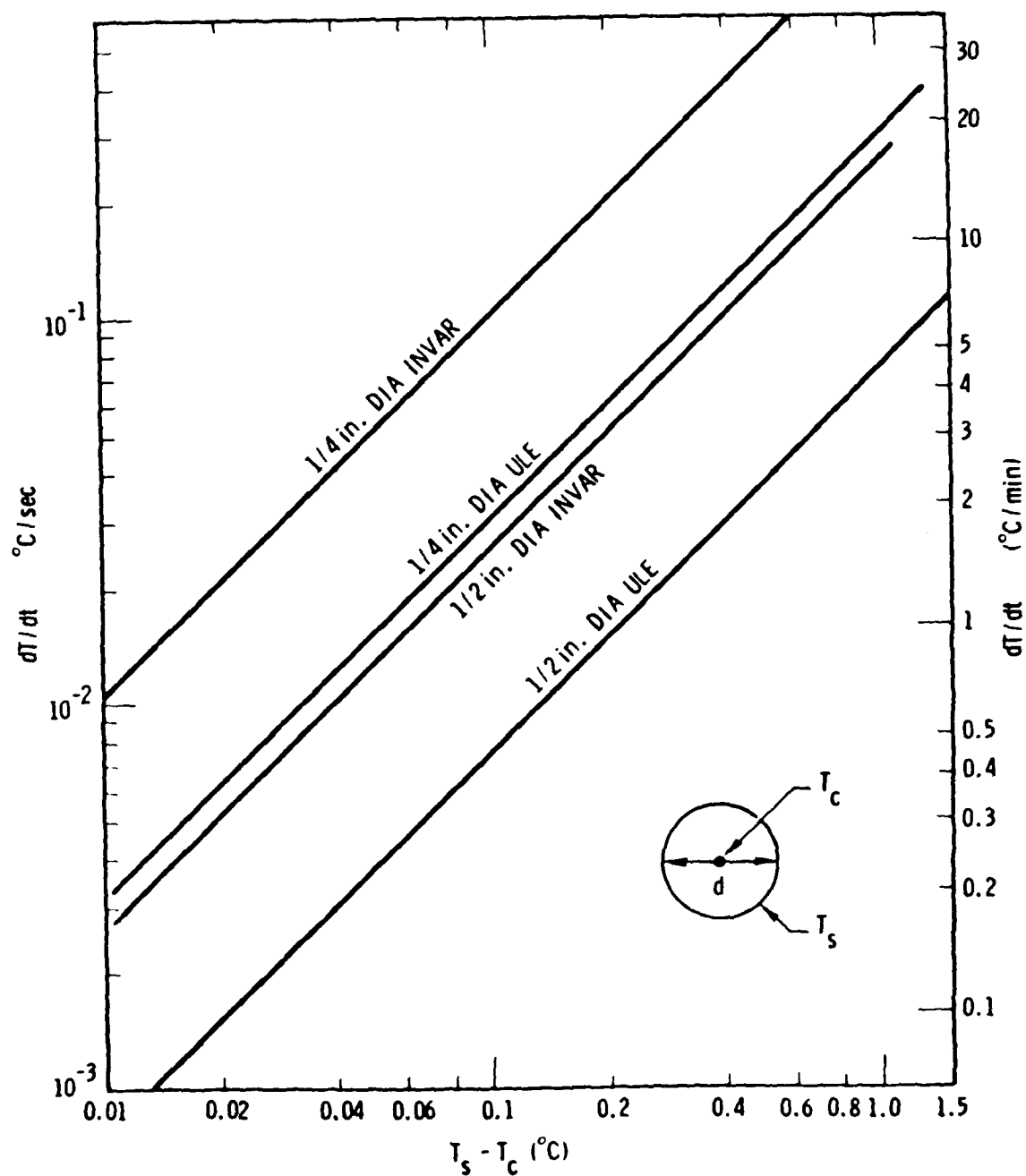


Figure 2. Variation of Radial ΔT with Heating and Cooling Rate

D. OPERATIONAL PROCEDURE

The general procedure for maximizing the signal-to-noise ratio is as follows: the main laser beams are first aligned without the sample or the PZT mirrors, so that the back reflections are close to, but not into, the beam laser exit cavity. This involves adjusting the first beam splitter position. The sample is inserted (with the heater/cooler removed) and the main beam is checked so that it clears the sample. The two beams over the sample are checked for overlap while the reference mirrors are temporarily removed. The reference mirrors are reinserted and the PZT mirrors are adjusted so that the beams $\overrightarrow{B_1 B_2}$ and $\overrightarrow{P_1 P_2}$ are parallel (with the sample in place). The sample's orientation is adjusted by means of the horizontal Invar rods so that a fringe pattern above either beam splitter (B_1 or B_2) is obtained; the other side should then require minimal adjustments. The photodetectors are then inserted and final adjustments are made, using the oscilloscope signals to maximize the ellipse or circle pattern.

III. SIGNAL PROCESSING

The fringe patterns are initially analyzed with S/P beam splitters and silicon photodiodes (Figs. 1 and 3). The PhotopTM UDT-455 detector/amplifier system (Silicon Photodetector Corp.) produces a voltage output that is typically ± 5 V with a good reflection and a 0.5-mW single-frequency He-Ne laser. This signal can be monitored in two ways, with either a dc or an ac approach, and in both cases the photodetector signals are applied to the x-y inputs of two oscilloscopes. A $\lambda/2$ fringe translation produces a 360° trace that is usually elliptical and can be adjusted with $\lambda/4$ plates. In the dc approach, either signal from each interferometer is plotted directly on a strip chart recorder. A third pen is used to record temperature.

Air is briefly introduced into the vacuum chamber and the direction of signal motion around the ellipse on the scope is recorded and correlated with the strip chart motion. An increase in the index of refraction is equivalent to an increase in the longer arm of each interferometer. This is equivalent, in turn, to reducing the shorter arm if "n" remains constant, and this establishes the direction of motion on each sample end face. This method allows for continuous tracking of very weak signals, the limit being determined by sample vibrations caused by the mechanical vacuum pump.

The major drawback is that readjustment of the optics after a signal is lost may switch the polarizations and hence the apparent direction of sample movement. The signals are also unsuitable for automatic data processing. Even if the sample expands or contracts linearly with temperature and time, the individual end faces will move in arbitrary directions as a result of the friction caused by the sample weight on its supports. Continuous analysis of all four photodetector signals would yield sample expansion data only if the signal amplitude were constant (which is rarely the case because of the small sample motions involved). Nevertheless, this method allows an operator to extract all the needed phase information after the experiment, from the sinusoidal traces on the chart.

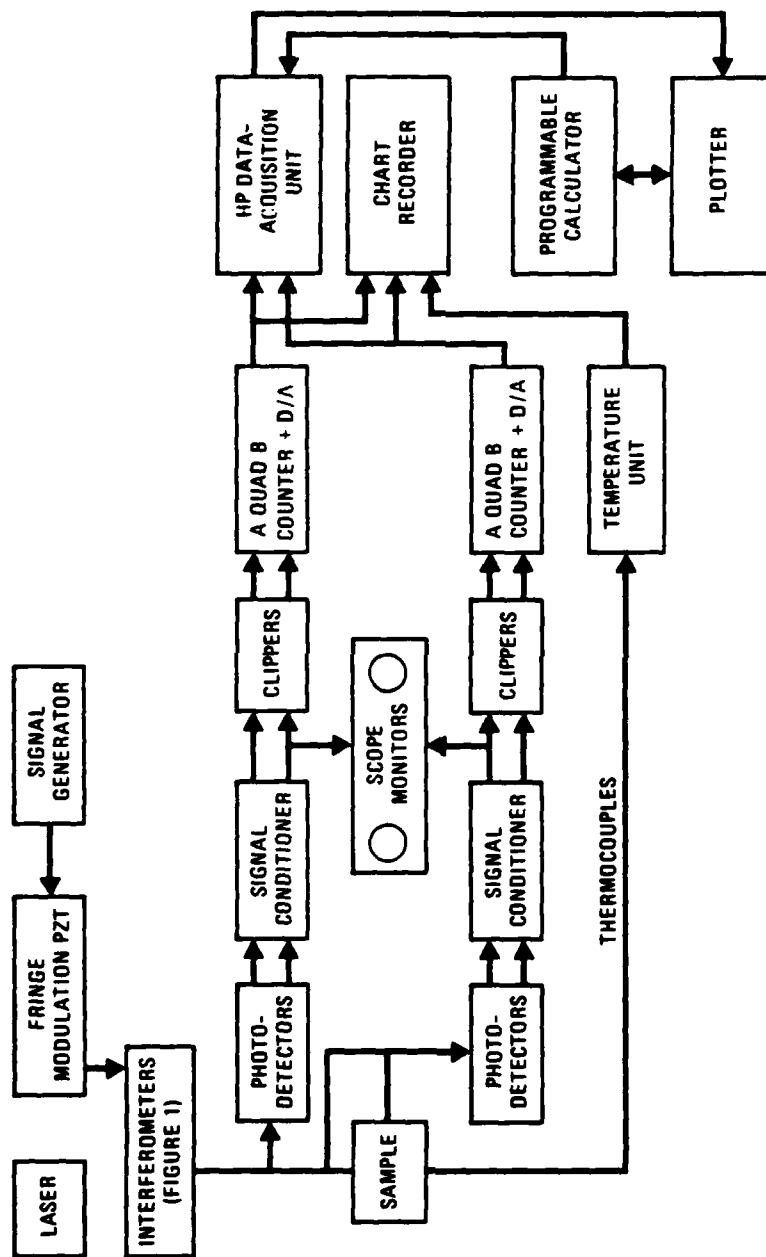


Figure 3. Block Diagram of the Test Setup for the Interferometric Dilatometer

An ac method was developed that requires only that the operator occasionally adjust the optics to maintain a minimum ellipse size on the oscilloscopes. This minimum size depends on the signal-to-noise ratio (which is related to sample reflectance, beam alignment, and sample vibrations). Below the minimum size the counter (described below) starts skipping counts, a phenomenon that is readily detectable from a discontinuity on the strip chart recorder.

A microprocessor can be readily programmed to correct for a discontinuity. The range of useful signal amplitudes varies typically from ± 5 V to a few mV. If a minimum signal cannot be regained by adjustment of the optics (e.g. mirrors B and P), the switch "S" in Fig. 4 converts over to the dc system and the dc offset is adjusted manually.

In the ac method, the PZTs in Fig. 1 are oscillated at a total displacement of just under $\lambda/2$, so that an almost-closed ellipse is displayed on each scope. A sawtooth rather than square wave input to the PZT is helpful. The frequency chosen (from 60 to 100 Hz) is based on a spectrum analysis of the mechanical system and represents a minimum extraneous noise region and an achievable PZT displacement. Direction of motion is determined by applying a dc voltage to each PZT and correlating changes in interferometer arm length.

The counting method is a scanning technique involving zero crossings and averaging for fringe interpolation. Advantages over phase-modulated techniques^{8,9} include simplified electronics and the use of interchangeable PZTs operating at low frequencies. This technique is sensitive only to gross shocks to the system that cause optical misalignment. Tuning of frequencies is unnecessary, as the fringe pattern is scanned in a manner duplicating the actual vibration-caused scanning. On the debit side, two photodetectors are still needed per interferometer and the state of polarization must be adjusted. Also, frequency response is lower, reducing one's ability to study simultaneous crack formation in materials.¹

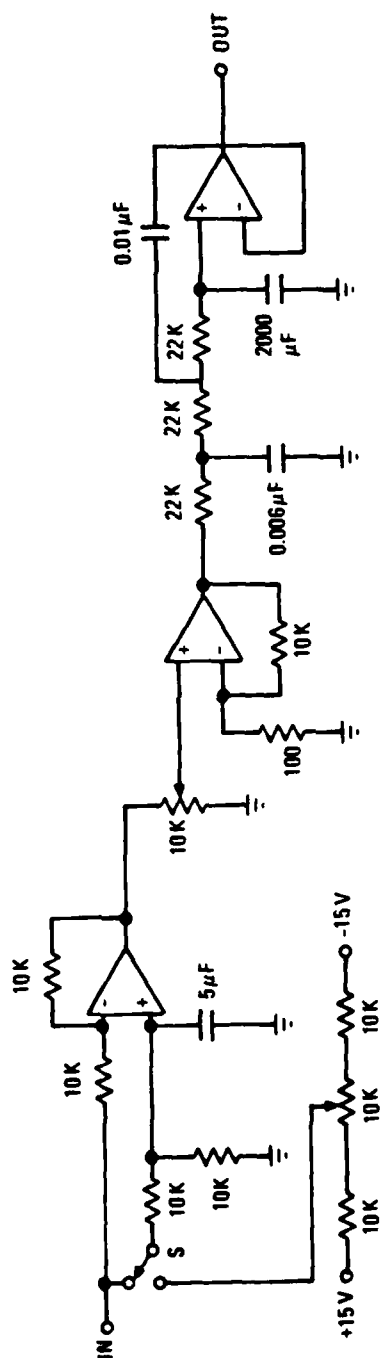


Figure 4. Schematic of the Interferometer Signal Conditioner (x4 for Double Michelson)

IV. AC COUNTER ELECTRONICS

Figure 3 illustrates schematically the automated ac counting system. This consists of (a) a signal conditioner (Fig. 4), (b) clippers (Fig. 5), and (c) quadrature counters with digital-to-analog (D/A) converters (Fig. 6). The latter provide data suitable for microprocessor analysis (see Section V).

The signal conditioner consists of a three-stage signal-conditioning network. The photodetector output has both ac and dc components. The 22- μ F capacitor cancels out the dc level when switch "S" is closed, so that the ac components will be centered around ground. This is a high-pass filter that eliminates signals <0.5 Hz. The next stage is a noninverting variable-gain amplifier that sets the conditional signal at any desired level. This is followed by a third-order low-pass filter that cancels out all frequencies >1 kHz. It was found that if filtering about the modulator frequency is too narrow, some of the phase information in the x-y signals is distorted. The low-pass filter suppresses high-frequency noise spikes that interfere with the directional counters.

The clipper circuit in Fig. 5 converts the amplified filtered sine-wave signals to a fixed square-wave output having a value of 5 V maximum when the sine wave input is above 0 V, and a 0 V output when the input drops below 0 V. The conditioner signals are first fed into a buffer amplifier and then clipped at 5 V by a Zener diode that interfaces with the logic gates. The square-wave signals are fed into Schmitt trigger NAND gates (#74132) for further waveform conditioning.

In the A quad B counter (Fig. 6), the square waves are time and phase analyzed by a series of one-shots and logic gates. The one-shots respond to the signal quadrant crossings by producing short pulses at the square-wave signal transitions. These pulses are directionally routed by the logic steering gates into the appropriate up or down counter inputs. With the aid of Boolean algebra¹⁴ in Fig. 7, it can be shown how the logic steering gates and one-shots function for different counting states. The circuit shows the

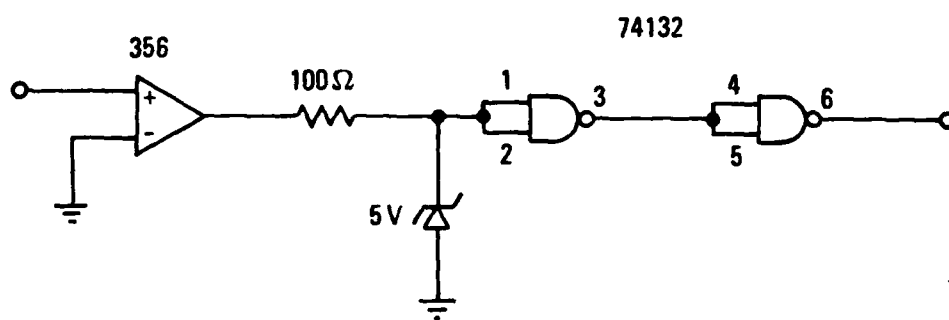


Figure 5. Schematic of the Clipper Circuit

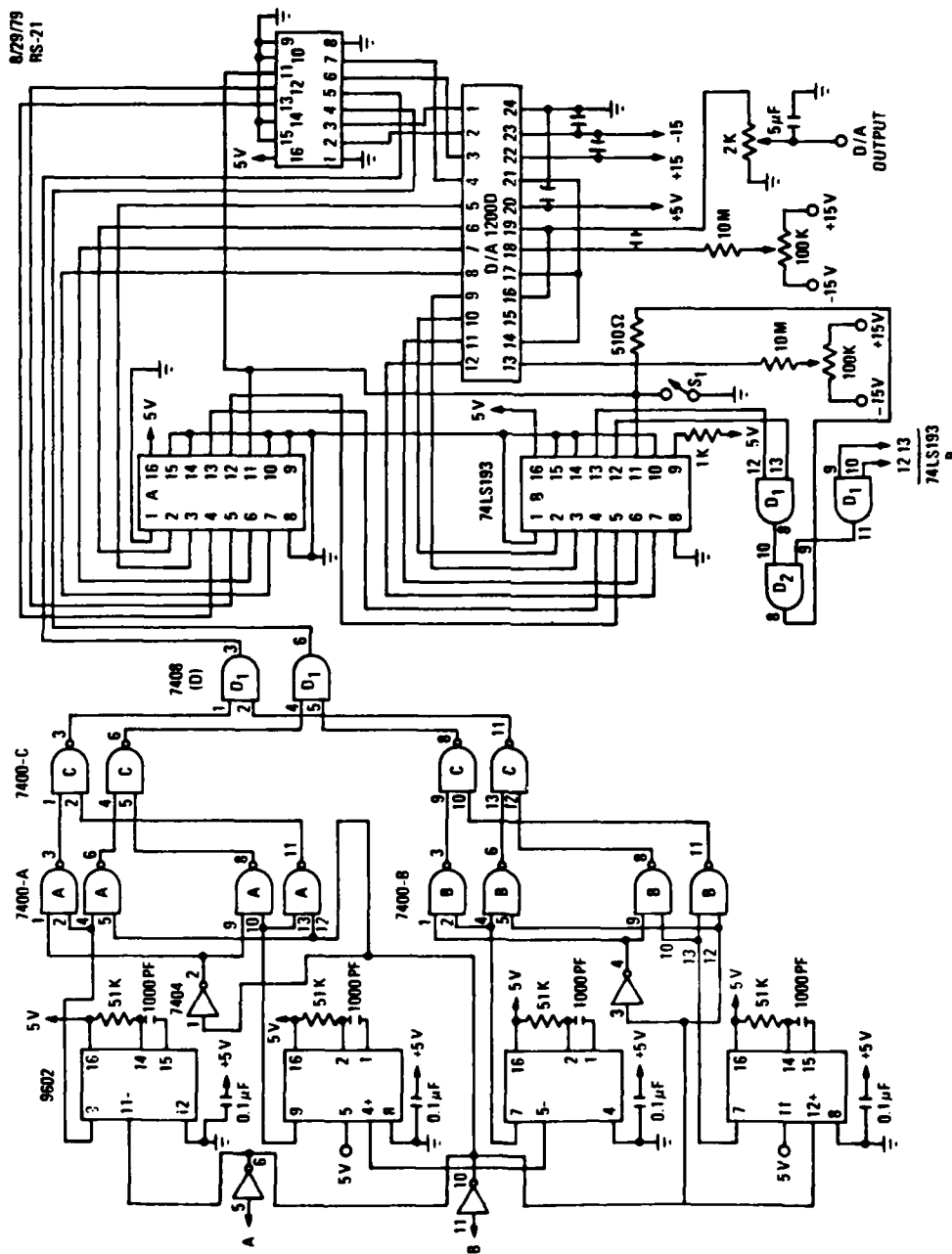


Figure 6. Schematic of the A Quad B Counter and the D/A Converter

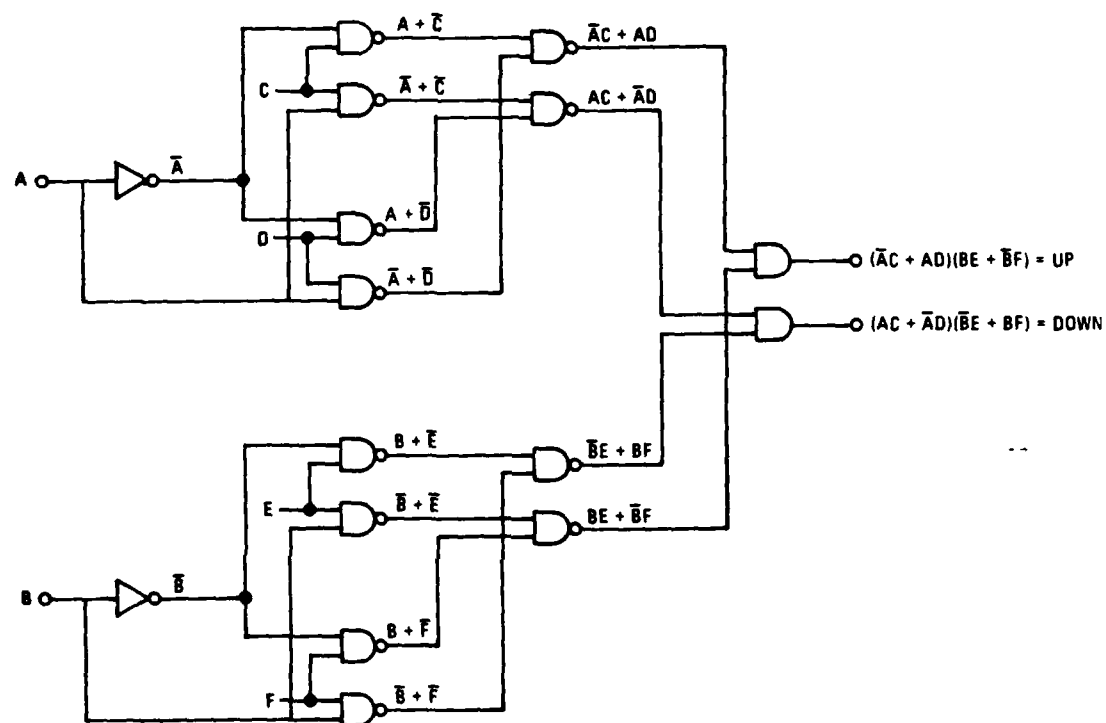


Figure 7. Schematic of the Steering Logic Circuit

letters A and B representing the clipped photodetector signals, and the letters C, D, E, and F representing the one-shot short-pulse transition signals. Figure 8 shows that the one-shots respond to the two counting conditions that can occur. By substituting the logic level values for any time t into each appropriate letter of the output Boolean expression, one can determine the circuit output response at any given time. An evaluation of the two counting states in Table 1 shows how the final up and down outputs respond to the clockwise and counterclockwise interferometer fringe signals (A and B). The direction of counting is determined by which clock input is pulsed with a low-to-high transition while the other clock input is high for the up/down counter.

The analog-to-digital (A/D) converter employs a 12-bit binary base and is used in a half full-scale output state. Thus, at half full scale the output total is ± 1024 counts. With one fringe ($\lambda/2$) equaling 4 counts, the counting range is reduced to ± 256 fringes before reset.

Table 1. Logic Circuit Evaluation

Case I @ t_1

A = 1	UP = $(\bar{A}C + AD)(BE + \bar{B}F)$	DOWN = $(AC + \bar{A}D)(\bar{B}E + BF)$
B = 0	= $(T \cdot 1 + 1 \cdot 1)(0 \cdot 1 + \bar{0} \cdot 0)$	= $(1 \cdot 1 + \bar{1} \cdot 1)(\bar{0} \cdot 1 + 0 \cdot 0)$
C = 1	= $(0 \cdot 1 + 1)(0 + 1 \cdot 0)$	= $(1 + 0 \cdot 1)(1 \cdot 1 + 0)$
D = 1	= $(0 + 1)(0 + 0)$	= $(1 + 0)(1 + 0)$
E = 1	= $1 \cdot 0$	= $1 \cdot 1$
	= 0	= 1

Case II @ t_2

A = 0	UP = $(\bar{A}C + AD)(BE + \bar{B}F)$	DOWN = $(AC + \bar{A}D)(\bar{B}E + BF)$
B = 1	= $(\bar{0} \cdot 1 + 0 \cdot 0)(1 \cdot 1 + \bar{1} \cdot 1)$	= $(0 \cdot 1 + \bar{0} \cdot 0)(\bar{1} \cdot 1 + 1 \cdot 1)$
C = 1	= $0 \cdot 1 + 0)(1 + 0 \cdot 1)$	= $(0 + 1 \cdot 0)(0 \cdot 1 + 1)$
D = 0	= $(1 + 0)(1 + 0)$	= $(0 + 0)(0 + 1)$
E = 1	= $1 \cdot 1$	= $0 \cdot 1$
	= 1	= 0

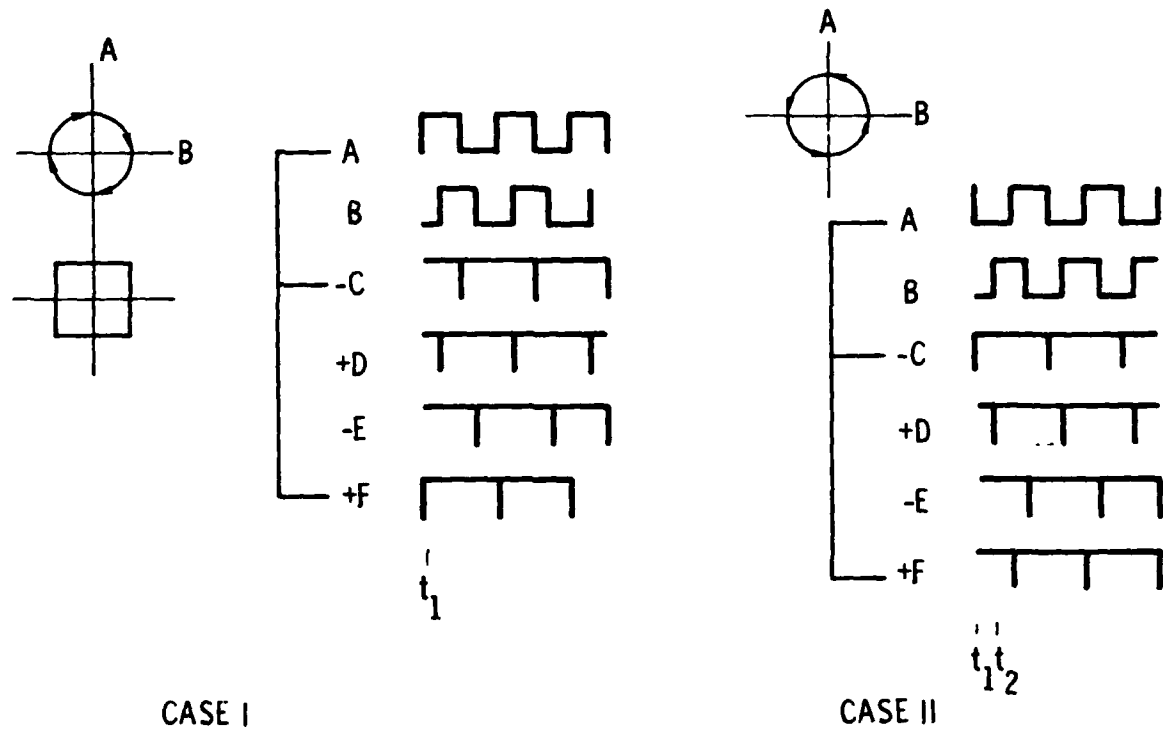


Figure 8. Diagram of the Directional Counting Sequence

Figures 9 and 10 represent the counter output when a mirror was placed against the window of one interferometer (Fig. 1) and a dc voltage was applied to the PZT (Burleigh PZ40), thereby moving the mirror P at $\sim 45^\circ$ to the beam. The counter was set at $10 \text{ mV} = \lambda/2 = 3164 \text{ \AA}$ by calibration with 360° circle rotation on the scope. The change in optical path-length difference (OPLD), proportional to the counter output, is given by

$$\Delta\text{OPLD} = 10^4 \phi V (\sin\theta)^{-1} \quad (7)$$

where ϕ is the PZT characteristic ($\sim 0.015 \text{ }\mu\text{m/V}$) and θ the beam incidence angle on mirror P. Figure 9 shows that the output corresponds initially to $\theta \sim 45^\circ$, but its curve is nonlinear and typically also shows hysteresis on voltage reversal. Figure 10 shows that over small distances (e.g. 2000 \AA), the counter follows the motion to within $\pm 15 \text{ \AA}$. When the PZT is replaced by a movable micrometer (Newport Res. Corp. model DM-13 on a model 430 stage, with fine adjustment of $0.1 \text{ }\mu\text{m}$) at $\sim 90^\circ$ to the beam, the curve is more linear. Figure 11 shows that the counter output (\AA) = $144.54 + 0.866$ (micrometer motion in \AA) with a correlation coefficient $r^2 = 0.99926$ over $3.5 \text{ }\mu\text{m}$.

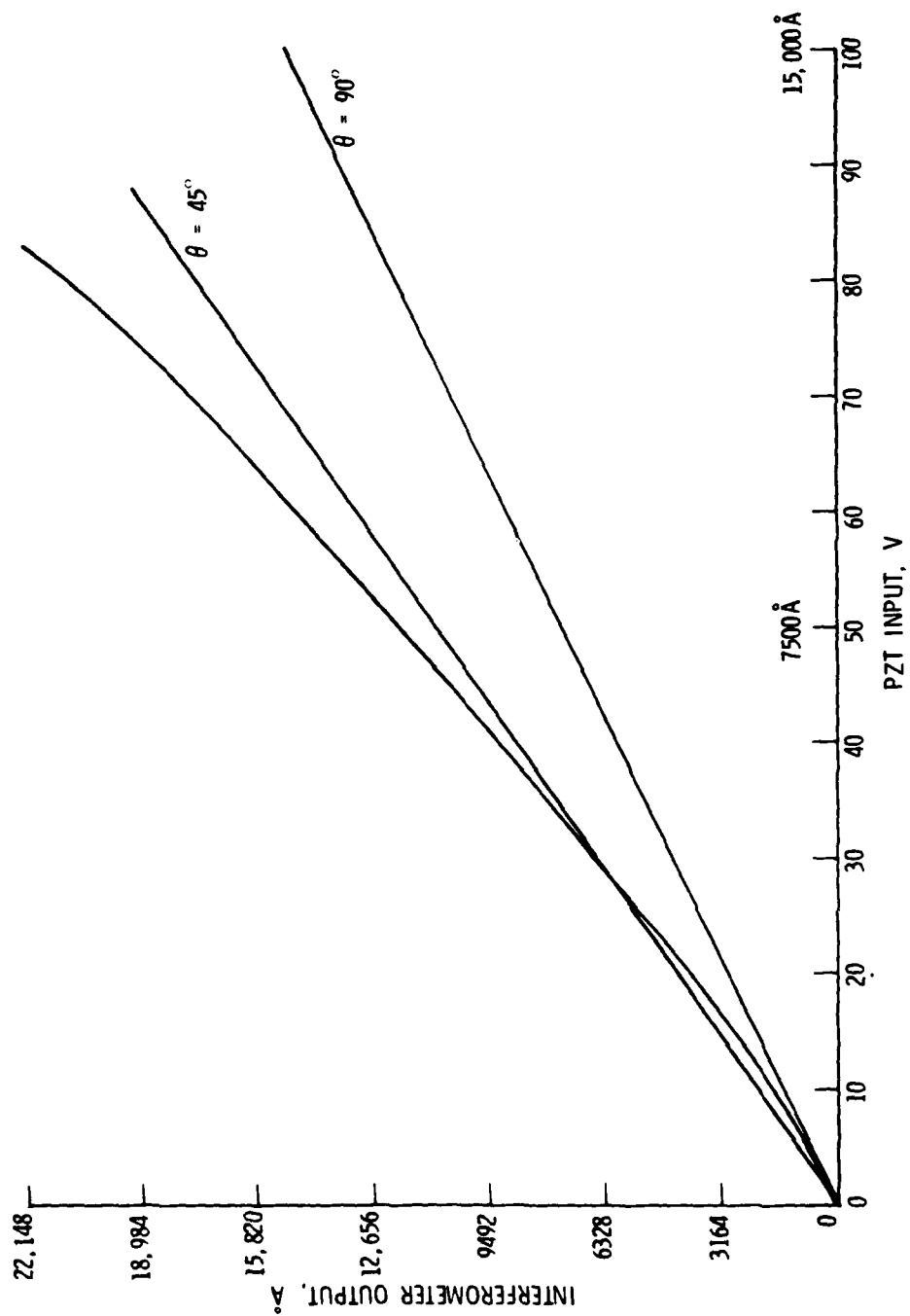


Figure 9. Interferometric Counter Output as Voltage Applied to PZT-Driven Mirror (1000 V \equiv 15 μ m motion)

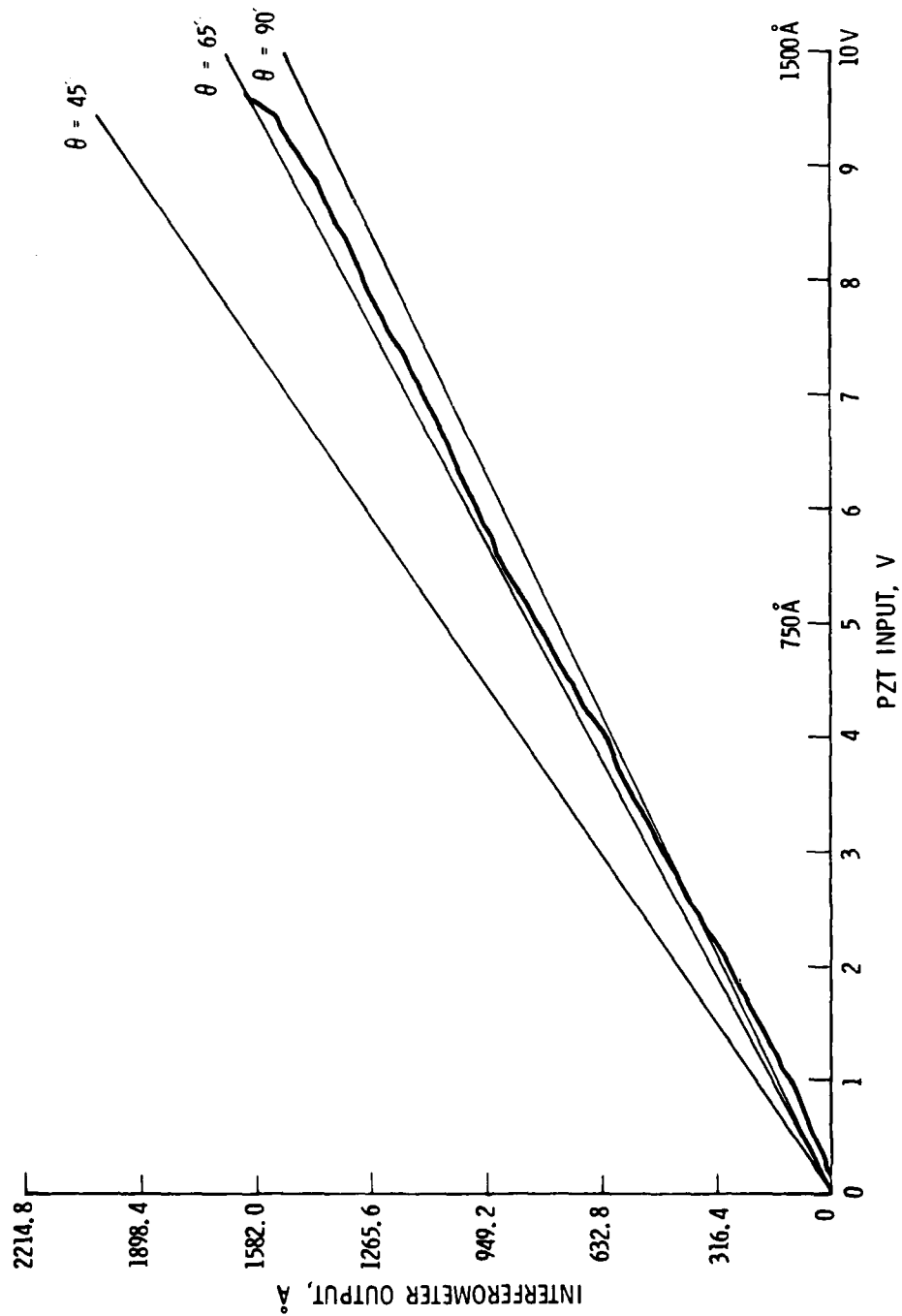


Figure 10. Interferometric Counter Output vs. Voltage Applied to PZT-Driven Mirror (fine scale)

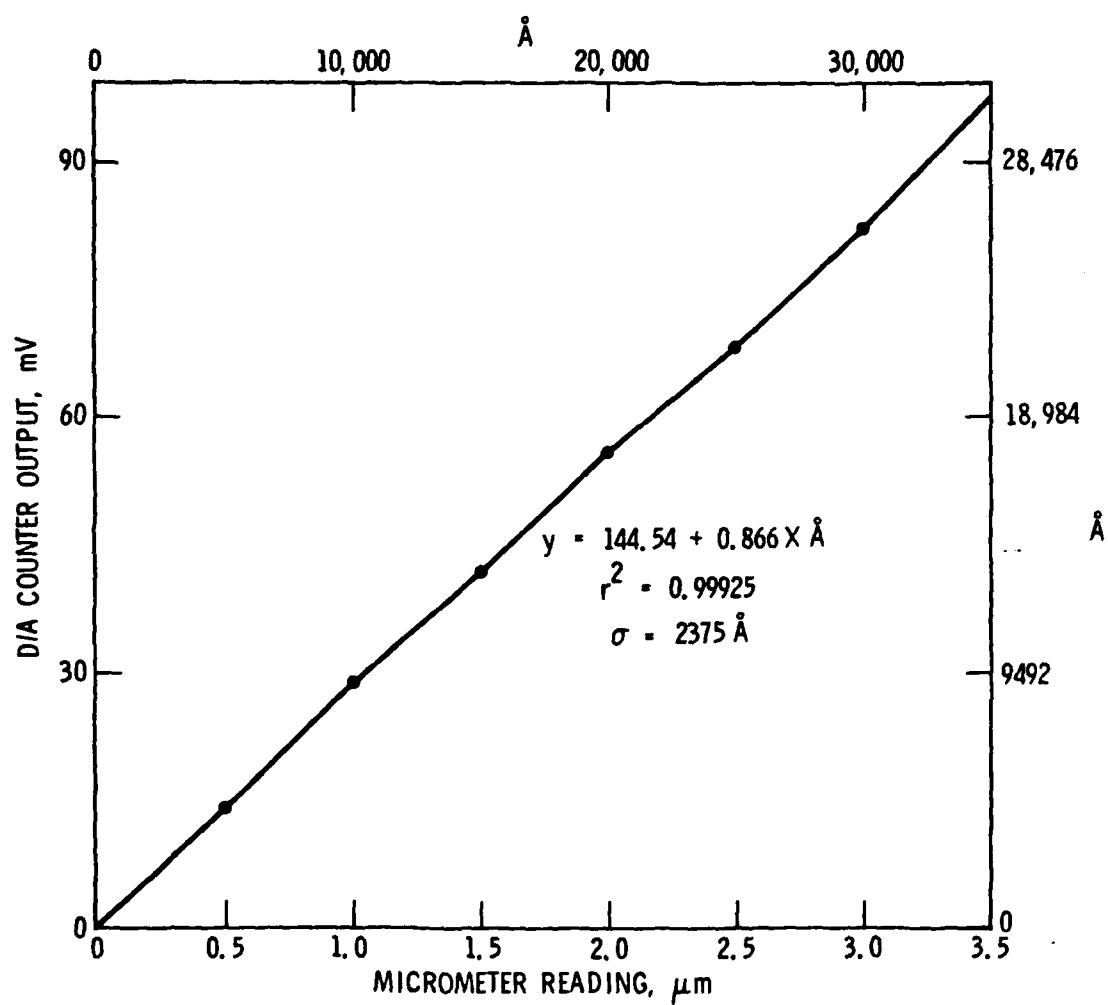


Figure 11. Counter Output vs. Micrometer Displacement

V. DATA PROCESSING

Thermal expansion characteristics are time-dependent for many materials; Fig. 2 indicated that low conductivity materials may not reach thermal equilibrium in a CTE test. Creep effects occur in many composites and visco-elastic materials, and time-dependent information regarding those effects is incorporated here by sampling the two interferometric counter outputs and analog temperature signals at regular intervals, using a timer module in a Hewlett-Packard HP1L system. An HP41CV calculator guides data acquisition and processing of the signals at intervals from >30 s, resulting in real-time instantaneous plots of $\Delta L/L$ and CTE versus temperature. Deviations from smooth curves can be correlated with point spacing and the heating or cooling rate.

The calculator is also used to correct for counting errors caused by extreme line-voltage surges, mechanical shocks, or very low signal-to-noise ratios (when optics realignment is indicated). For example, a critical voltage is set in the calculator program. If a reading exceeds the previous one by this value, the program discards that reading and plots instead an extrapolated one based on three (or more) former readings. These previous readings are then "shifted" to the level of the actual signal so that subsequent readings are unaffected. At the same time, this extrapolation gives an instantaneous CTE.

Figure 12 illustrates these features for a quartz rod that was first cooled from ambient temperature, then heated to ~ 400 K and cooled back to ambient. The main hysteresis is caused by thermal lag of the inside of the rod and is diminished by slower cooling rates. An initial setting of 8 for the exponent for CTE proved too sensitive, and a switch to 7 on heating improved the data display. (These values were plotted per individual data point; averaging over several data points permits use of the 8 scale). (The occasional discontinuities in the $\Delta L/L$ curve are results without the corrections described above). A wider range of instantaneous CTEs is recorded whenever the temperature trend is reversed or isothermal data are desired.

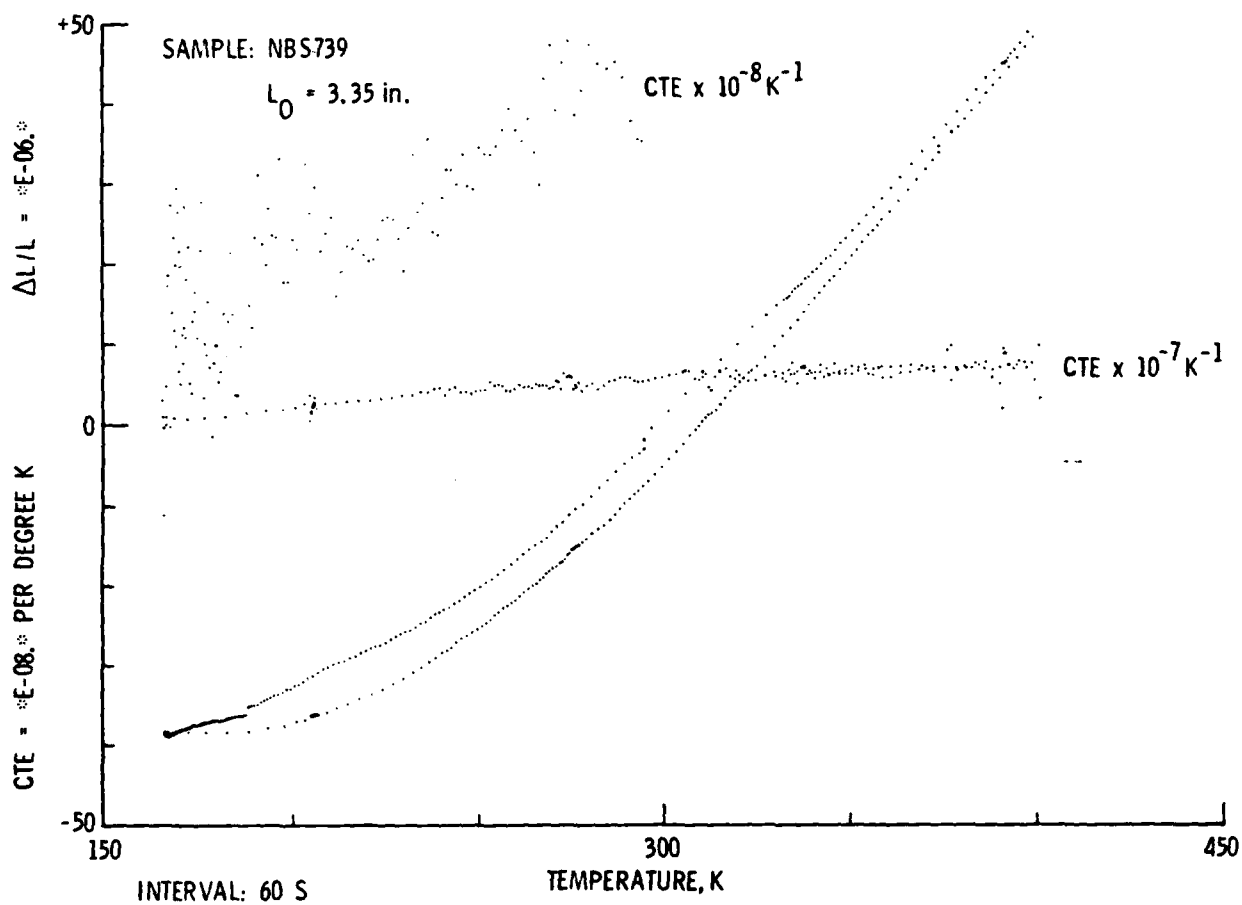


Figure 12. Thermal Strain and Instantaneous CTE vs. Temperature for a Fused-Silica Rod

VI. CONCLUSIONS

The optical, signal processing, and data reduction systems of a precision double Michelson interferometer have been described. Real-time thermal strain and instantaneous CTEs can be measured for a sample of arbitrary size or shape for temperatures from 100 to >450 K. An inexpensive signal processor permits data sampling at regular intervals, in order to present simultaneous time-dependent behavior. $\Delta L/L$ can be recorded to a precision of about $\pm 15 \text{ \AA}$, and the CTE (a slope of 3 $\Delta L/L$ points, typically a 4° spread) can be measured to $\pm 5 \times 10^{-8} \text{ K}^{-1}$.

Further improvements in both accuracy and resolution are possible by using nonmechanical vacuum pumps alone, optical isolators for the lasers, improved line voltage, stabilization, and precise design of the \overrightarrow{BP} path, to minimize the effects of ambient air-temperature fluctuations.

REFERENCES

1. E. G. Wolff, "Materials and Processes - On-Service Performance," National SAMPE Technical Conference Series, Vol. 9 (1977), pp. 57-72.
2. E. G. Wolff and S. A. Eselun, Rev. Sci. Instr. 50, 502 (1979).
3. E. G. Wolff and S. A. Eselun, Proc. SPIE 192, 204 (1979).
4. L. E. Drain, J. H. Speake, and B. C. Moss, "Displacement and Vibration Measurement by Laser Interferometry," SPIE Vol. 136, 1st European Congress on Optical Metrology (1977).
5. A. P. Miller and A. Cezairliyan, Thermal Expansion 6, ed. I. D. Peggs (Plenum Press, 1978), pp. 131-143.
6. Y. Souche, R. Vergne, J. C. Cotillard, J. L. Porteseil, G. Roblin, and G. Nomarski, "A High-Sensitivity Polarization Interferometry Dilatometer," 8th Int. Thermal Expansion Symposium, NBS (June 1981).
7. W. D. Drotning in Thermal Expansion 7, ed. D. C. Larsen, (Plenum Press, 1982); also, SANDIA Report SAND 83-0197, UC-37 (May 1983).
8. S. A. Eselun and E. G. Wolff, ISA Trans. 19 (1), 58-64 (1980).
9. S. A. Eselun, R. C. Savedra, and E. G. Wolff, "Analysis and Design of a New Phase-Modulated Michelson Interferometer," Air Force Space Division Rept. SD-TR-81-113, (18 December 1981).
10. E. G. Wolff and S. A. Eselun, U. S. Patent No. 4,313,679, (2 February 1982).
11. E. G. Wolff, B. K. Min, and M. H. Kural, "Thermal Cycling of a Unidirectional Graphite/Magnesium Composite," J. Mat. Science (1984), to be published.
12. J. C. Owens, Appl. Opt. 6 (1), 57 (1967).
13. E. G. Wolff, E. G. Kendall, and W. C. Riley, "Thermal Expansion Measurements of Metal-Matrix Composites," in Advances in Composite Materials - ICCM3, Vol. 2, ed. A. R. Bunsell et al. (1980), pp. 1140-1152.
14. R. J. Tocci, Digital Systems (Prentice Hall, N.J., 1977), Chap. 2.

LABORATORY OPERATIONS

The Laboratory Operations of The Aerospace Corporation is conducting experimental and theoretical investigations necessary for the evaluation and application of scientific advances to new military space systems. Versatility and flexibility have been developed to a high degree by the laboratory personnel in dealing with the many problems encountered in the nation's rapidly developing space systems. Expertise in the latest scientific developments is vital to the accomplishment of tasks related to these problems. The laboratories that contribute to this research are:

Aerophysics Laboratory: Launch vehicle and reentry fluid mechanics, heat transfer and flight dynamics; chemical and electric propulsion, propellant chemistry, environmental hazards, trace detection; spacecraft structural mechanics, contamination, thermal and structural control; high temperature thermomechanics, gas kinetics and radiation; cw and pulsed laser development including chemical kinetics, spectroscopy, optical resonators, beam control, atmospheric propagation, laser effects and countermeasures.

Chemistry and Physics Laboratory: Atmospheric chemical reactions, atmospheric optics, light scattering, state-specific chemical reactions and radiation transport in rocket plumes, applied laser spectroscopy, laser chemistry, laser optoelectronics, solar cell physics, battery electrochemistry, space vacuum and radiation effects on materials, lubrication and surface phenomena, thermionic emission, photosensitive materials and detectors, atomic frequency standards, and environmental chemistry.

Computer Science Laboratory: Program verification, program translation, performance-sensitive system design, distributed architectures for spaceborne computers, fault-tolerant computer systems, artificial intelligence and microelectronics applications.

Electronics Research Laboratory: Microelectronics, GaAs low noise and power devices, semiconductor lasers, electromagnetic and optical propagation phenomena, quantum electronics, laser communications, lidar, and electro-optics; communication sciences, applied electronics, semiconductor crystal and device physics, radiometric imaging; millimeter wave, microwave technology, and RF systems research.

Materials Sciences Laboratory: Development of new materials: metal matrix composites, polymers, and new forms of carbon; nondestructive evaluation, component failure analysis and reliability; fracture mechanics and stress corrosion; analysis and evaluation of materials at cryogenic and elevated temperatures as well as in space and enemy-induced environments.

Space Sciences Laboratory: Magnetospheric, auroral and cosmic ray physics, wave-particle interactions, magnetospheric plasma waves; atmospheric and ionospheric physics, density and composition of the upper atmosphere, remote sensing using atmospheric radiation; solar physics, infrared astronomy, infrared signature analysis; effects of solar activity, magnetic storms and nuclear explosions on the earth's atmosphere, ionosphere and magnetosphere; effects of electromagnetic and particulate radiations on space systems; space instrumentation.

LABORATORY OPERATIONS

The Laboratory Operations of The Aerospace Corporation is conducting experimental and theoretical investigations necessary for the evaluation and application of scientific advances to new military space systems. Versatility and flexibility have been developed to a high degree by the laboratory personnel in dealing with the many problems encountered in the nation's rapidly developing space systems. Expertise in the latest scientific developments is vital to the accomplishment of tasks related to these problems. The laboratories that contribute to this research are:

Aerophysics Laboratory: Launch vehicle and reentry fluid mechanics, heat transfer and flight dynamics; chemical and electric propulsion, propellant chemistry, environmental hazards, trace detection; spacecraft structural mechanics, contamination, thermal and structural control; high temperature thermomechanics, gas kinetics and radiation; cw and pulsed laser development including chemical kinetics, spectroscopy, optical resonators, beam control, atmospheric propagation, laser effects and countermeasures.

Chemistry and Physics Laboratory: Atmospheric chemical reactions, atmospheric optics, light scattering, state-specific chemical reactions and radiation transport in rocket plumes, applied laser spectroscopy, laser chemistry, laser optoelectronics, solar cell physics, battery electrochemistry, space vacuum and radiation effects on materials, lubrication and surface phenomena, thermionic emission, photosensitive materials and detectors, atomic frequency standards, and environmental chemistry.

Computer Science Laboratory: Program verification, program translation, performance-sensitive system design, distributed architectures for spaceborne computers, fault-tolerant computer systems, artificial intelligence and microelectronics applications.

Electronics Research Laboratory: Microelectronics, GaAs low noise and power devices, semiconductor lasers, electromagnetic and optical propagation phenomena, quantum electronics, laser communications, lidar, and electro-optics; communication sciences, applied electronics, semiconductor crystal and device physics, radiometric imaging; millimeter wave, microwave technology, and RF systems research.

Materials Sciences Laboratory: Development of new materials: metal matrix composites, polymers, and new forms of carbon; nondestructive evaluation, component failure analysis and reliability; fracture mechanics and stress corrosion; analysis and evaluation of materials at cryogenic and elevated temperatures as well as in space and enemy-induced environments.

Space Sciences Laboratory: Magnetospheric, auroral and cosmic ray physics, wave-particle interactions, magnetospheric plasma waves; atmospheric and ionospheric physics, density and composition of the upper atmosphere, remote sensing using atmospheric radiation; solar physics, infrared astronomy, infrared signature analysis; effects of solar activity, magnetic storms and nuclear explosions on the earth's atmosphere, ionosphere and magnetosphere; effects of electromagnetic and particulate radiations on space systems; space instrumentation.